Organic Electronics 129 (2024) 107048

Contents lists available at ScienceDirect

Organic Electronics

journal homepage: www.elsevier.com/locate/orgel

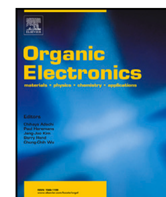

Research paper

Compact modeling of hysteresis in organic thin-film transistors ☆

A. Romero [a], J.A. Jiménez-Tejada [a,*], R. Picos [b], D. Lara [a], J.B. Roldán [a], M.J. Deen [c]

[a] Departamento de Electrónica y Tecnología de Computadores, CITIC-UGR, Universidad de Granada, Granada 18071, Spain
[b] Department of Industrial Engineering and Construction, Universitat de les Illes Balears, Palma 07122, Illes Balears, Spain
[c] Department of Electrical and Computer Engineering, McMaster University, 1280 Main Street West, Hamilton, Ontario L8S 4K1, Canada

ARTICLE INFO

Keywords:
Compact modeling
Contact effects
Evolutionary parameter extraction method
Hysteresis
Thin-Film Transistors (TFTs)

ABSTRACT

In this work, we propose a model that describes the temporal evolution of the threshold voltage and trapped charge density in Thin-Film Transistors (TFTs) under dynamic conditions, paving the way for the characterization and modeling of memory transistors. The model is expressed as a first-order differential equation for the trapped charge density, which is controlled by a time constant and an independent term proportional to the drain current. The time-dependent threshold voltage is introduced in a previously developed compact model for TFTs with special consideration to the contact effects. The combination of both models and the use of an evolutionary parameter extraction procedure allow for reproducing the experimental dynamic behavior of TFTs. The results of the model and the evolutionary procedure have been validated with published experimental data of pentacene-based transistors. The procedure is able to simultaneously reproduce three kinds of experiments with different initialization routines and constraints in each of them: output and transfer characteristics with hysteresis and current transients characteristics.

1. Introduction

The rapid growth of information requires massive storage of data. Different memory designs are under development to cope with this demand, with organic technology being one of the candidate memory technologies. An important device in this technology is the organic thin-film transistor (OTFT) which inherits the advantages of its intrinsic material, such as mechanical flexibility and low-cost solution processability [1–7]. Different OTFTs are fabricated accordingly in order to adapt to current requirements in non-volatile memory applications [8]. In particular, these transistors are present in several types of non-volatile memories, such as the organic phase-change memory transistors (OPCMTs) [9], transistor-based organic flash memories [5,10], organic resistive random-access memories (RRAMs) [11–13], organic ferroelectric field-effect-transistors [14–17], and magnetoresistive random-access memory (MRAM) [18]. Organic devices can also be found in optoelectronic memory applications, used in image capturing, information recording, or logic data processing, where the devices combine the functions of electrical memory with photodetection [19–26].

Many of the memory transistors are based on hysteresis effects present in their electrical characteristics, in which the charge trapping at the semiconductor-dielectric interface in both metal-oxide-semiconductor field-effect transistors (MOSFETs) or TFTs plays an important role [23,25,27–31], apart from affecting its low-frequency noise and light-sensitive characteristics [19–22]. While it is considered a desirable feature in memory devices, hysteresis in the electrical characteristics of other devices can be a serious constraint, in particular in transistors in which electrical stability is a requirement for proper performance [32–34]. Hysteresis in transistors leads mainly to changes in the threshold voltage V_T, which can produce malfunction of logic and analog circuits, thus limiting their commercialization [35]. In any case, transistors with large or minimal hysteresis must be properly characterized in order to detect how large or small, respectively, are the changes in V_T. Additionally, in cases where charge trapping in the organic semiconductor (OSC) or interfaces are clearly the origin of the hysteresis [23,25,27–30,36,37], monitoring the changes of charge trapped concentration is highly desired.

The determination of changes in V_T from forward and reverse voltage scans is found in the literature [32,35,38]. Also, useful methods to determine the trap density in OTFTs have been proposed [39,40].

☆ The authors acknowledge support from the project PID2022-139586NB-44 funded by MCIN/AEI/10.13039/501100011033 and FEDER, EU. Funding for open access charge: Universidad de Granada / CBUA.

* Corresponding author.
E-mail addresses: adrianromerocaceres@gmail.com (A. Romero), tejada@ugr.es (J.A. Jiménez-Tejada), rodrigo.picos@uib.es (R. Picos), jroldan@ugr.es (J.B. Roldán), jamal@mcmaster.ca (M.J. Deen).

https://doi.org/10.1016/j.orgel.2024.107048
Received 18 January 2024; Received in revised form 13 March 2024; Accepted 2 April 2024
Available online 5 April 2024
1566-1199/© 2024 The Author(s). Published by Elsevier B.V. This is an open access article under the CC BY-NC-ND license (http://creativecommons.org/licenses/by-nc-nd/4.0/).

Nevertheless, it is difficult to find publications that keep track of the evolution of V_T or even the trapped charge concentration during the whole hysteresis cycle. Actually, these two magnitudes vary continuously from the beginning to the end of a hysteresis cycle, depending not only on the applied voltage or current, but also on the time used to perform the sweep.

In this work, we propose a model that describes the continuous evolution of V_T and trapped charge concentration along hysteresis cycles of the electrical characteristics of OTFTs. Our model can be incorporated in any compact model with an explicit dependence on V_T [41–45]. Here, we introduce our model in a previously developed compact model for OTFTs with special consideration to the contact effects [46–49]. The resulting combination of both models and the use of an evolutionary parameter extraction procedure allow for reproducing the experimental dynamic behavior of OTFTs [50].

In Section 2, the generic drift model, in which our proposal is inserted, is presented. In Section 3, we describe the dynamic model for V_T and trapped charge density. The evolutionary parameter extraction procedure is detailed in Section 4. The results are presented in Section 5, and finally the work is concluded in Section 6.

2. Generic drift model for OTFTs

We initially consider an unified compact model that describes the electrical characteristics of TFTs. It includes the effects of the intrinsic channel of the transistor and the source and drain contact regions (Fig. 1).

2.1. Model for the intrinsic region

The intrinsic channel is usually described with a generic charge drift model as [46,51–60]:

$$I_D = \mu_0 C_{ox} \frac{W}{L'} \frac{V_{EODR}(V_G, V_S)^{(2+\gamma)} - V_{EODR}(V_G, V_{D'})^{(2+\gamma)}}{2+\gamma},$$
$$L' = L/(1+\lambda|V_{D'} - V_S|),$$
$$V_{EODR}(V_G, V) = V_{SS} \ln\left[1 + \exp\left(\frac{V_G - V_T - V}{V_{SS}}\right)\right], \tag{1}$$

which includes an electric field dependent mobility

$$\mu = \mu_0 (V_G - V_T)^{\gamma}. \tag{2}$$

The model (1) uses the asymptotically interpolation function $V_{EODR}(V_G, V)$ in order to consider the sub-threshold regime, $V_{EODR}(V_G, V) \approx V_{SS} \exp[(V_G - V_T - V)/V_{SS}]$, as well as the above-threshold regime, $V_{EODR}(V_G, V) \approx (V_G - V_T - V)$, with either $V = V_S$ or $V = V_{D'}$, and V_{SS} is the sub-threshold swing of the TFT. The rest of variables are V_G, the gate terminal voltage, V_D, the drain terminal voltage, and V_S and $V_{D'}$ are the values of the potential at the edges of the intrinsic channel in contact with the source and drain regions, respectively. Thus, V_S is the voltage drop at the source contact and $V_{DD'} = V_D - V_{D'}$ is the voltage drop at the drain contact (Fig. 1). C_{ox} is the capacitance per unit area of the gate insulator and W and L are the channel width and length, respectively. L' is the effective channel length modulated by the coefficient λ. If the channel length modulation effect is negligible, λ can be assumed zero and $L' \approx L$, minimizing the computational time of (1). μ_0 is the mobility-related parameter expressed as $\mathrm{cm}^2/(\mathrm{V}^{1+\gamma}\mathrm{s})$, and γ is the mobility enhancement factor, suggested to depend on the characteristic energy width $E_0 = kT_0$ of an exponential tail distribution of the density of states (DOS) and the absolute temperature T, and $\gamma = 2(T_0/T - 1)$ [61]. In order to provide a single value for the voltage dependent mobility, the mobility is evaluated at $V_{GT} = V_G - V_T = 1$ V, thus $\mu(V_{GT} = 1\ \mathrm{V}) = \mu_0$ in $\mathrm{cm}^2/(\mathrm{Vs})$. Model (1) is able to describe all operation modes of the transistor: triode, saturation, sub-threshold or even reverse biasing.

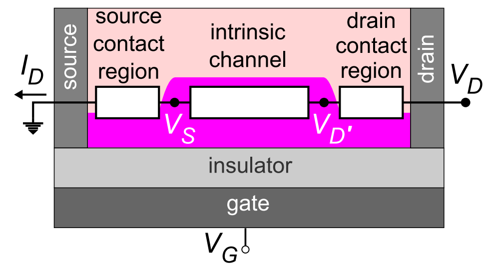

Fig. 1. Modeling the contact regions and intrinsic channel of an OTFT structure (a bottom-contact configuration). Usually $V'_D = V_D$ [62].

2.2. Model for the contact regions

The model for the intrinsic channel (1) is completed with another model that describes the electrical characteristics of the drain and source contact regions. Although the model (1) is prepared to consider the drain and source contact effects, in most OTFTs, the drain contact effects are negligible, as potentiometry measurements showed in Ref. [62]. In this work, we consider these cases because it simplifies the modeling and characterization of OTFTs since $V_{DD'} \approx 0$ V and $V_D \approx V_{D'}$, and only the source contact model is necessary.

A versatile model that was successfully tested in different situations [48,49], and is capable of describing both space-charge-limited transport in low energy contact-barriers [47] and injection-limited transport in Schottky barriers [56,63–65], is:

$$I_D = M_S \times V_S{}^{m_s},$$
$$\forall m_s \in \mathbb{Z} : 0 < m_s \leq 2, \tag{3}$$

where m_s is a constant, independent of V_G, and its value makes the model (3) discern among injection-limited transport in Schottky barriers [$0 < m_s < 1$, with (3) being a convex function]; space-charge-limited transport [$1 < m_s \leq 2$, with (3) being a concave function], in which the particular value $m_s = 2$ transforms (3) into the classical Child's law; and finally, the value $m_s = 1$ corresponds to Ohmic contacts, in which I_D and V_S are linearly related:

$$I_D = V_S / R_S, \tag{4}$$

where R_S is the source contact resistance. In this last case, the parameter M_S coincides with the contact conductance: $M_S = 1/R_S$. The parameter M_S in (3) was proposed to depend on V_G as [47]:

$$M_S = \alpha_s (V_G - V_T)^{1+\gamma}, \tag{5}$$

where α_s is a proportionality constant. Studies analyzing Ohmic contacts [41] or non-linear ones justify this dependence with V_G [38,47,53,54,66–68]. This electric field dependence of M_S, which was physically justified for $m_s = 1$ (Ohmic contacts) [47] and $1 < m_s \leq 2$ (space-charge-limited contacts) [47], was later assumed and checked for $0 < m_s < 1$ (Schottky contacts) [48]. The sub-threshold regime can be incorporated into (5) by an asymptotically interpolation function [54], similar to the one used in V_{EODR}(1):

$$M_S = \alpha_s \left\{ V_{SS} \ln\left[1 + \exp\left(\frac{V_G - V_T}{V_{SS}}\right)\right]\right\}^{1+\gamma}. \tag{6}$$

Note that in some staggered configurations, the voltage drop at the drain contact may not be negligible [57,69,70]. For these situations, the drain contact model would be necessary as was detailed in [49].

The generic drift model (1)–(6) presented so far does not take into account trapping and de-trapping effects which would make parameters V_T and V_{SS} change. To address this issue, models for V_T and V_{SS} as a function of the trapped charge and time are formulated in the following section.

3. Dynamic behavior of the trapped charge density

3.1. Threshold voltage V_T and V_{SS}

Any shift in the threshold voltage ΔV_T caused by a variation of trapped charge in the semiconductor layer, insulator, or the interface between the insulator and the semiconductor $q\Delta n_{t1}$, with n_{t1} in cm^{-2}, can be expressed as [71–73]:

$$\Delta V_T = -\frac{q\Delta n_{t1}}{C_{ox}}, \tag{7}$$

where q is the free carrier charge.

The sub-threshold swing V_{SS} is also prone to changes with the density of trapped charge in bulk traps n_{t_b} or in interface traps n_{t_i} [74]. Assuming these densities independent of energy, the sub-threshold swing may be written as [75]:

$$V_{SS} = \frac{kT}{q}\ln 10 \times \left(1 + \frac{q}{C_{ox}}(\sqrt{\varepsilon_s n_{t_b}} + q n_{t_i})\right). \tag{8}$$

This expression is simplified by defining an equivalent trapped charge density per unit area and unit energy, n_{t2} in cm^{-2} eV^{-1}, [40]:

$$V_{SS} = \frac{kT}{q}\ln 10 \times \left(1 + \frac{q^2}{C_{ox}} n_{t2}\right). \tag{9}$$

Thus, their variations are related as:

$$\Delta V_{SS} = \frac{kT}{q}\ln 10 \times \left(\frac{q^2 \Delta n_{t2}}{C_{ox}}\right). \tag{10}$$

Note that the values of n_{t1}(cm^{-2}) in (7) and n_{t2}(cm^{-2} eV^{-1}) in (9) would be the same for a deep trap located in a 1 eV semiconductor bandgap. Thus, for typical semiconductor gaps, a usual estimation found in the literature is $n_{t1}(\text{cm}^{-2}) \approx n_{t2}(\text{cm}^{-2}\ \text{eV}^{-1})$ [76–78].

In the following, we define a generic trapped carrier density n_t in (cm^{-2} or cm^{-2} eV^{-1}), which magnitude n_t(cm^{-2} or cm^{-2} eV^{-1})$\equiv n_{t1}$(cm^{-2})$\approx n_{t2}$(cm^{-2} eV^{-1}) and its associated trapped charge density $Q_t \equiv q n_t$ in (C cm^{-2} or C cm^{-2} eV^{-1}). These variables can vary along the channel, thus the mean values along the channel should be considered instead. The mean value of Q_t is defined as:

$$Q_{tL} = \frac{1}{L}\int_0^L Q_t \mathrm{d}x. \tag{11}$$

With these definitions, the values of V_T and V_{SS} at a particular instant t_j can be related to their values at a previous instant t_{j-1} from (7) and (10), respectively as:

$$V_T(t_j) = V_T(t_{j-1}) - \left[\frac{Q_{tL}(t_j) - Q_{tL}(t_{j-1})}{C_{ox}}\right], \text{ and} \tag{12}$$

$$V_{SS}(t_j) = V_{SS}(t_{j-1}) + \frac{kT}{q}\ln 10 \times \left[q\frac{Q_{tL}(t_j) - Q_{tL}(t_{j-1})}{C_{ox}}\right], \tag{13}$$

with Q_{tL} in C cm^{-2} in (12) and Q_{tL} in C cm^{-2} eV^{-1} in (13), as described above.

3.2. Model for Q_t

In this section, we propose a semi-empirical model that describes the evolution of the trapped charge in the transistor as a response to changes of the voltages applied to the external terminals, V_G and V_D. Two generic scenarios can affect the dynamic response of the trapped charge in the transistor, which are found in any protocol that analyzes the dynamic response of a transistor [50,79].

(i) $V_D = 0\,\text{V}$, and thus, $I_D = 0\,\text{A}$. The distributions of free and trapped charges are uniform across the channel length L of the transistor (see Fig. 2(a)). Variations in the trapped charge are produced only by changes in V_G. Once V_G changes, Q_t evolves to a new steady state, at a rate controlled by a time constant τ, as:

$$\frac{\mathrm{d}Q_{tL}}{\mathrm{d}t} = -\frac{Q_{tL}(t) - Q_{t0}}{\tau}, \tag{14}$$

where $Q_{t0} = Q_{t0}(V_G)$ is the steady state value of Q_t at V_G.

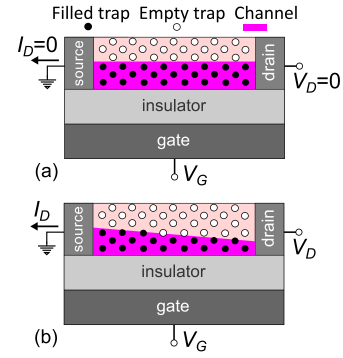

Fig. 2. (a) Uniform and (b) non-uniform channels.

Eq. (14) can be solved at discrete instants, allowing to calculate Q_{tL} at an instant t_j for a number of traps n_{traps} (each one with a different time constant τ_r) as

$$\begin{aligned} Q_{tL}(t_j) &= \sum_{r=1}^{n_{traps}} Q_{tL_r}(t_j), \\ Q_{tL_r}(t_j) &= Q_{tL_r}(t_{j-1})e^{-\frac{t_j - t_{j-1}}{\tau_r}} + Q_{t0_r}(1 - e^{-\frac{t_j - t_{j-1}}{\tau_r}}), \end{aligned} \tag{15}$$

and $Q_{t0_r} = qN_{T_r}y_G$,

where N_{T_r} is the concentration per unit volume of trap r, and $y_G = y_G(V_G)$ is the thickness of the intrinsic channel with free carriers and filled traps.

(ii) $V_D \neq 0\,\text{V}$ and $I_D \neq 0\,\text{A}$. The distributions of free and trapped charges are non-uniform across the channel length L of the transistor (see Fig. 2(b)). Variations in the trapped charge are produced by changes in any of the gate or drain voltages bringing the transistor into a new steady state. In addition, the flow of free charge carriers can be seen as a mechanism that favors the trapping, like a generation term in a continuity equation for trapped charges. In this regard, we propose this generation term to be proportional to I_D with a parameter β:

$$\frac{\mathrm{d}Q_{tL}}{\mathrm{d}t} = \beta I_D - \frac{Q_{tL}(t)}{\tau}. \tag{16}$$

Eq. (16) can be solved for discrete instants, allowing to calculate Q_{tL} at an instant t_j for n_{traps} traps (each one with a different time constant τ_r, with $r = 1 \ldots n_{traps}$) as

$$\begin{aligned} Q_{tL}(t_j) &= \sum_{r=1}^{n_{traps}} Q_{tL_r}(t_j), \text{ and} \\ Q_{tL_r}(t_j) &= Q_{tL_r}(t_{j-1})e^{-\frac{t_j - t_{j-1}}{\tau_r}} + \beta_r \tau_r I_D(1 - e^{-\frac{t_j - t_{j-1}}{\tau_r}}). \end{aligned} \tag{17}$$

A physical justification of the model described in (14) and (16) can be found in Appendix A.

4. Evolutionary parameter extraction procedure

4.1. Individual representation

This section complements the previous two ones by presenting an evolutionary procedure that allows for the determination of the individual of the population, x, which is the set of parameters needed to compute all the equations of the model (1), (3), (6), (12) and (13), (15) and (17):

$$x = (\mu_0, \gamma, V_T(0), V_{SS}(0), m_s, \alpha_s, \lambda, s, Q_{tL}(0), \beta, \tau). \tag{18}$$

where $Q_{tL}(0) = (Q_{tL,1}, \ldots, Q_{tL,n_{traps}})$ (see (S3) in the Supporting Information (SI)) defines the initial values of the trapped charge in a different number of traps, n_{traps}, with also different associated parameters $\tau =$

$\tau_1, \ldots, \tau_{n_{traps}}$ and $\beta = \beta_1, \ldots, \beta_{n_{traps}}$; $V_T(0)$ and $V_{SS}(0)$ are the initial values of $V_T(t)$ and $V_{SS}(t)$, respectively, for a specific experiment; and parameter s controls a smooth transition from conduction towards the depletion regime. This transition is only detected well below the subthreshold regime, usually in the transfer characteristics (see SI Section S1).

The starting point to determine the individual x is an evolutionary parameter extraction procedure developed in the previous publications [48,49,54,80–82]. A primary objective of this evolutionary procedure is to automate the decision-making, thus reducing the work of the expert or decision maker (DM) during a parameter extraction. For completeness, the main steps of this procedure are described in the next sub-sections.

In this work, the equations that handle the impact of hysteresis in TFTs [(12), (13), (15) and (17)] have been incorporated in the last version of the compact model [49]. Moreover, the original evolutionary parameter extraction procedure [53] is adapted in this work to reproduce, using the bisection method [53,82,83], three different kinds of measurements: $I_D - V_D$ and $I_D - V_G$ curves of OTFTs with hysteresis and $I_D - t$ transients.

4.2. Measurement discretization and timing

In the first place, the experimental I_D, in any of its forms, output or transfer characteristics, or current transients, must be referred to the time instants t_j at which all the measurements are taken, $I_D = I_D(V_G(t_j), V_D(t_j))$, where $j \in \mathbb{Z} : 1 \le j \le t_N$, and t_N is the total number of discrete values of t. The relations $V_G(t_j)$ and $V_D(t_j)$ define the measurement protocol or routine that must be followed in order to obtain reproducible and reliable measurements. The parameter extraction procedure must also adapt to the exact timings of this protocol, which is described in Section S2 and Fig. S2 for the measurements used in this work [50,79]. The numerical estimation of I_D with our model (1), (3), (6), (12), (13), (15) and (17) is named $\widehat{I_D}(V_G(t_j), V_D(t_j), x)$.

4.3. Fitness function

The evolutionary parameter extraction procedure solves a multi-objective problem (MOP) [82] with three objectives (O_1, O_2 and O_3), in order to find the values of the set of parameters in x, where (O_1) refers to output characteristics, (O_2) transfer characteristics, and (O_3) current transients. The three of them aim to minimize the error (O_k), with $k = 1 \ldots 3$, between the experimental values of $I_D = I_D(V_G(t_j), V_D(t_j))$ and their estimation $\widehat{I_D}(V_G(t_j), V_D(t_j), x)$ from (1), (3), (6), (12), (13), (15) and (17).

The *Normalized Root Mean Squared Error* (NRMSE) is used to estimate the errors (O_1), (O_2) and (O_3) [84]:

$$\mathrm{NRMSE}(y, \hat{y}) = \sqrt{\frac{\sum_{z=1}^{w} (y_z - \hat{y}_z)^2}{\sum_{z=1}^{w} (y_z - \bar{y})^2}}, \tag{19}$$

where y represents the data set that we want to accurately approximate, $\hat{y}$ is the estimation of y, w is the number of data samples in y, and $\bar{y}$ is the mean value of the complete data set y.

Thus, our minimization multi-objective optimization problem (MOP), named O, is defined as $O = (O_1, O_2, O_3)$, where

$$O_k(x) = \mathrm{NRMSE}\left(I_D(V_G(t_j), V_D(t_j)), \widehat{I_D}(V_G(t_j), V_D(t_j), x) \right), \quad k = 1, 2, 3. \tag{20}$$

Objectives (O_1), (O_2) and (O_3) allow us to accurately reproduce experimental $I_D - V_D$, $I_D - V_G$ and $I_D - t$ curves, respectively, introducing the parameters coded in x into our model.

4.4. Search space definition

The definition of a proper search space is essential in order to save computing time costs. The presence of hysteresis makes this task more complex. Gathering information about similar samples in previous works can help. It is also advisable to start using less accurate methods (in particular, when hysteresis is present) to extract some of the parameters of the model, such as the application of the traditional MOS model and the H_{VG} method [85]. They can provide an initial estimation of μ_0, γ and V_T [48,49,53,54,82,86]. Also, current transients can be fitted with n_{traps}-order exponential decay functions to estimate the value of the time constants τ_r of the n_{traps} traps. Finally, with the gathered information, the decision maker is in charge of defining physically valid search ranges for each parameter of x [53].

4.5. Constraints

It is worth mentioning that certain parameter constraints are implicit in the search space definition, which must be consistent with the physical meaning of each parameter. Other constraints need to be added to the procedure [49]. This is the case of the sign of the trapped charge. Assuming hole traps in p-type transistors and electron traps in n-type ones, the values of the trapped charge are restricted to:

$Q_{tL}(t_j) \ge 0$ for p-type devices

$Q_{tL}(t_j) \le 0$ for n-type devices

$\forall t_j \ge 0.$

5. Results

The evolutionary procedure summarized in the previous section is applied to the electrical characteristics ($I_D - V_D$, $I_D - V_G$ and $I_D - t$) shown with symbols in Figs. 3(a)–3(b), 4(a) and 5(a), respectively. The analysis of these three experiments has been carried out using an open source evolutionary tool called ECJ (A Java-based Evolutionary Computation Research System) [87]. The model formula and data extraction code can be found in the supplementary material. They were measured in a bottom-gate, bottom-contact pentacene-based p-type FET with SiO_2 as the gate dielectric [50]. Drain/source electrodes, Cr (5 nm) and Au (40 nm), where Cr acts as an adhesion layer, are deposited through a shadow mask. The device has a channel length and width of $L = 26$ μm and $W = 2000$ μm, respectively. The electrode deposition, substrate cleaning and surface passivation descriptions are given in [50].

The scan rate in experiments $I_D - V_D$ and $I_D - V_G$ is 5 V/100 ms, and the elapsed time between two consecutive measurements is $\Delta t = 100$ ms [50,79]. The total time for the combined sequence of nested sweep measurements shown in Figs. 3(a)–3(b) is 34.2 s, including a hold time, $t_{hold} = 3$ s [50,79], or elapsed time at $V_D = 0$ V between the point at which V_G is changed to a new value, and the point at which V_D starts being swept (see Fig. S2a). The measurement time for the combined forward and backward sweeps in Fig. 4(a) is 4 s [50,79] (see Fig. S2b). In the $I_D - t$ transients, the time between two consecutive measurements is $\Delta t = 25$ s, and the total measurement time for the combined current transients in Fig. 5(a) is 1000 s [50,79] (see Fig. S2c).

Note that the model is developed for N-type TFTs, in which I_D, V_D and V_G are positive in the above-threshold mode. In P-type TFTs, I_D, V_D and V_G are frequently expressed and represented with negative values. The best way to cope with this sign difference for P-type TFTs is: (i) to change the sign of the experimental values of I_D, V_D and V_G, (ii) to work with the equations of the model like a N-type transistor, and (iii), when all the analysis is finished, to change again the sign of I_D, V_D and V_G and also the sign of the resulting values of V_T and V_{SS}.

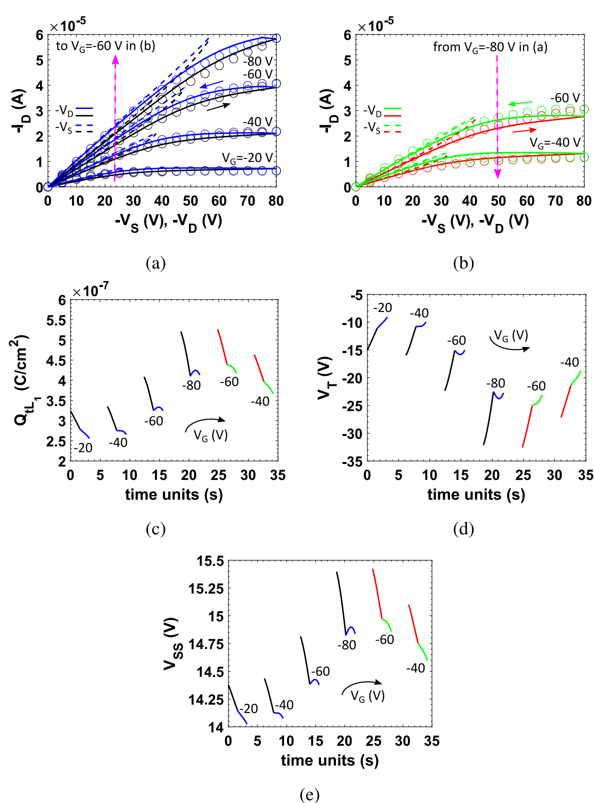

Fig. 3. (a),(b) Comparison of experimental output characteristics of a pentacene based field effect device [50] (symbols), with our calculations (solid lines), using the parameters of Table 1 and the time evolution of (c) Q_{tL_1}, (d) V_T and (e) V_{SS} described by relations (12), (13) and (15). The dashed lines correspond to V_S described by model (3). The evolution of Q_{tL_1}, V_T and V_{SS} are deliberately not shown during the waiting times (t_{hold} = 3 s) at V_D = 0 V. Exponential decays following (17) would appear in the blank gaps connecting the final and initial ends of the successive $I_D - V_D$ sweeps. V_G is swept from OFF-to-ON and back from ON-to-OFF following this sequence of values: −20, −40, −60, −80 V (depicted in (a)), −60 and −40 V (depicted in (b)). Black and red lines in all the figures indicate that V_D is swept from 0 to −80 V. Blue and green lines indicate that V_D is swept back from −80 to 0 V.

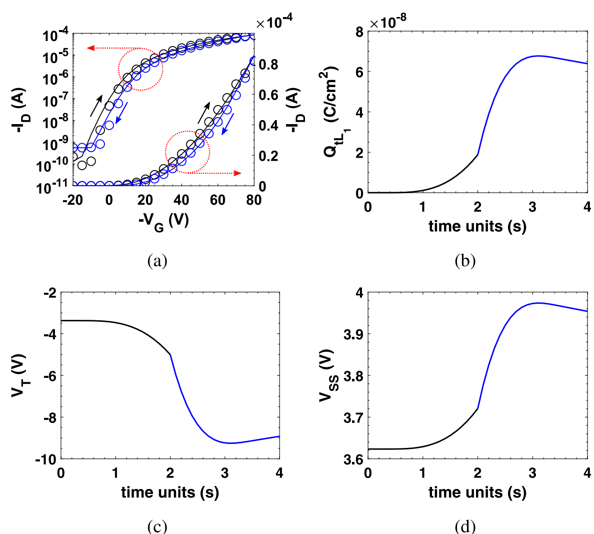

Fig. 4. (a) Comparison of experimental transfer characteristics (in linear and logarithmic scales) of the pentacene based transistor of Fig. 3 [50] (symbols), with our calculations (lines), using the parameters of Table 1 and the time evolution of (b) Q_{tL_1}, (c) V_T and (d) V_{SS} described by relations (12), (13), (15) and (17). Black lines in all the figures indicate that V_G is swept from +20 to −80 V; and the blue lines indicate that V_G is swept back from −80 to +20 V. V_D = −80 V.

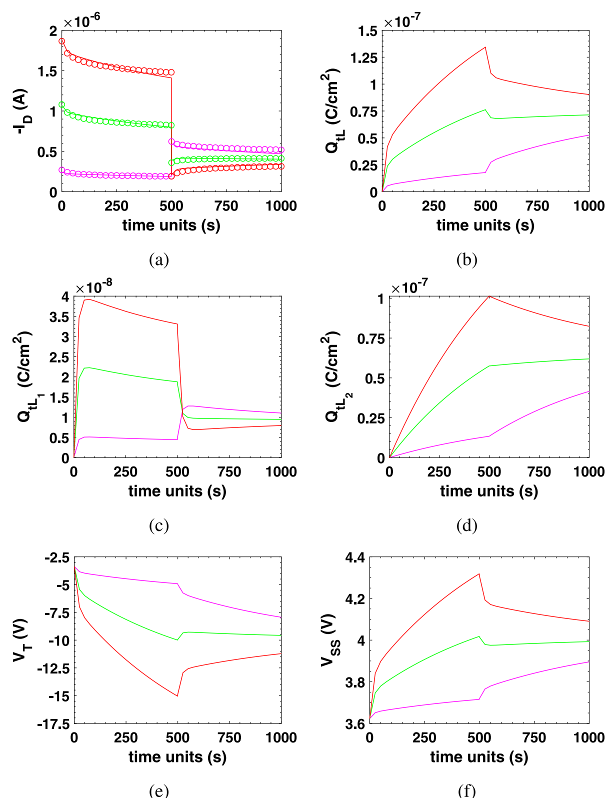

Fig. 5. (a) Comparison of experimental (symbols) and our calculated (lines) $I_D - t$ transients for the pentacene transistor of Figs. 3 and 4 monitored for 1000 s, where V_G = +50 V when $t < 0$; V_G = −50 (red), −30 (green) and −10 V (pink) when $0 < t < 500$ s; and V_G = −20 V when $t > 500$. V_D = −10 V. Our calculations use the parameters of Table 1 and the evolution of (b) $Q_{tL_1} + Q_{tL_2}$, (c) Q_{tL_1}, (d) Q_{tL_2}, (e) V_T and (f) V_{SS} described by (12), (13) and (17).

5.1. Specification of the individual

Before applying the procedure, the exact relation of the device's parameters included in the individual x (18) must be defined for the specific sample and measurements to be analyzed. Table 1 shows the relation of the parameters used in the fitting of the experimental curves in Figs. 3(a)–3(b), 4(a) and 5(a). The checked boxes in this table point out the parameters that are needed in the fitting of any of the three electrical characteristics. An explanation of why these parameters are necessary is given below.

The first point is the determination of the number of traps n_{traps} participating in the trapping processes. It is difficult to guess the number of traps from the output or transfer characteristics. In order to detect the existence of different traps with short and long time constants, time dependent current transients are needed [50]. Then, the transients can be fitted with a second order exponential decay function [30]. From the analysis of the experimental current transients, shown with symbols in Fig. 5(a), two traps, n_{traps} = 2, were expected [50]. The detection of trap #2 was possible because, in the range $500 < t < 1000$ s, the three transients of Fig. 5(a) can be fitted with a two-term exponential decay function such as $A_k + B_k \exp(-t/\tau_1) + C_k \exp(-t/\tau_2)$ ($k = 1 \ldots 3$) [50]. If A_k, B_k, C_k are determined independently in each of the three transients, a first estimation of the time constants would be τ_1 = 10 s and τ_2 = 140 s (Fig S4a and Table S1). If a more physical condition for A_k is imposed, i.e. A_k must be the same, then τ_1 = 100 s and τ_2 = 5000 s (Fig. S5 and Table S2). These values for the time constants define a starting point from which our procedure will search for the optimum values. The trap #1 with the shortest time constant, τ_1, is considered in the analysis of the three $I_D - V_D$, $I_D - V_G$ and $I_D - t$ curves (parameter x_{15} in Table 1).

The trap #2, with longer time constant τ_2 (parameter x_{16} in Table 1), is only included in the $I_D - t$ curves, since the total measurement time is much shorter in the $I_D - V_D$ and $I_D - V_G$ curves than in the $I_D - t$ curves.

The parameters associated with the traps needed to solve Eq. (16) are β, or β_r with $r = 1, 2$, and the initial value of the trapped charge at the beginning of any experiment $Q_{tL}(0)$, or $Q_{tL_r}(0)$ with $r = 1, 2$. It would be desirable to use a common value for β_r for all the experiments. However, the physical meaning of β extracted from (A.17) would make this parameter dependent on the local electric field along the channel. In this sense, it is preferable to split this parameter into different ones according to the type of experiment: (a) V_G is constant and V_D is variable, such as output characteristics in forward and backward sweeps ($\beta_{r_{o,f}}$ and $\beta_{r_{o,b}}$, respectively, for trap #r); and (b) V_D is constant and V_G is variable, such as transfer characteristics, in forward and backward sweeps ($\beta_{r_{t,f}}$ and $\beta_{r_{t,b}}$, respectively, for trap #r); and current transients, only in forward mode ($\beta_{r_{t,f}}$ for trap #r). Since trap #1 is considered in all the experiments and trap #2 only in the current transients, five β parameters are needed: $\beta_{1_{o,f}}$, $\beta_{1_{o,b}}$, $\beta_{1_{t,f}}$, $\beta_{1_{t,b}}$ and $\beta_{2_{t,f}}$ ($x_8, \ldots, x_{12}$ in Table 1).

The initial value of the trapped charge also depends on the type of experiment since the initialization routine is different (see Section S2 and Fig. S2). In the output characteristics, the value of V_G is held during some seconds at $V_D = 0\,\text{V}$, before V_D is swept. At $t = 0\,\text{s}$, the first value of V_G is well above V_T. Thus, there are free carriers in the intrinsic channel, and traps in this region are expected to be filled during this first hold time at the beginning of the experiment. Then, $Q_{tL}(0) = Q_{tL,1} \neq 0$ C/cm^2 for trap #1, but its value is unknown (parameter x_{17} in Table 1). In the transfer characteristics and current transients, the initial value of V_G is well below V_T. Thus, there are no free charges, the traps are empty and $Q_{tL}(0) = 0$ C/cm^2 in these two experiments (trap #1 in the transfer characteristics and traps #1 and #2 in the current transients). Therefore, there is no need to introduce any additional parameter when these initial values are known.

Since the occupation of the traps is different at the beginning of the $I_D - V_D$ experiment in comparison to the beginning of both $I_D - V_G$ and $I_D - t$ experiments, the initial values of $V_T(0)$ and $V_{SS}(0)$ must accordingly be different. In this regard, V_{T_o} (x_3) and V_{SS_o} (x_5) are their respective initial values in the $I_D - V_D$ experiment, and V_{T_t} (x_4) and V_{SS_t} (x_6) are their respective initial values in both $I_D - V_G$ and $I_D - t$ experiments.

The rest of the parameters of the individual x (see Table 1) are common parameters to all the experiments: charge-carrier mobility related parameters μ_0 and γ (x_1 and x_2, respectively); source-contact related parameters α_s and m_s (x_7 and x_{13}, respectively); modulation channel length parameter $1/\lambda$ (x_{18}); and depletion-conduction transition related parameter s (x_{14}).

5.2. Fitting results

Once the parameters of the individual x (18) have been selected for each experiment, the evolutionary parameter extraction procedure must search for the value of all these parameters. In order not to enlarge the length of this paper, the main steps followed during a typical extraction procedure and the analyses carried out in the decision-making process are in the SI, in a flow chart in Fig. S3 and in Section S3. Similar steps and analyses are followed in the experiments of this work.

The best fitting obtained with the procedure is shown with solid lines in the Figs. 3(a)–3(b), 4(a) and 5(a). A very good agreement between the experimental and simulated data has been obtained using the parameters shown in Table 1. The common parameters extracted for all the experiments are $\mu_0 = 1.31$ cm^2/Vs (x_1), which agrees with the value of μ_0 reported in previous works [88,89]; $\gamma \approx 0$ (x_2), which is similar to $\gamma = 0.004$ reported in [38]; and $m_s \approx 1$ (x_{13}), indicating that the contact region is Ohmic. The voltage drop in the contact region takes a large part of the applied drain voltage, as can be seen in dashed lines in Figs. 3(a)–3(b). Finally, other common parameters are the time constants of the traps #1 and #2 detected in the experiments, $\tau_1 = 13.23$ s and $\tau_2 = 1000$ s, respectively. The difference between these final values of τ_1 and τ_2 and the starting values (extracted with the fitting of the current transients with a two-term exponential decay function (Tables S1 and S2)) is due to the fact that our method aims, not only to fit the transients in the whole range $[0, 1000]$ s, but also our procedure also fits the $I_D{-}V_D$ and $I_D{-}V_G$ experiments. As a test, current transients were calculated with our model, replacing the values of τ_1 and τ_2 in Table 1 with $\tau_1 = 10$ s and $\tau_2 = 140$ s. A poor fitting is expected, as seen in Fig. S4b.

Apart from the extraction of static parameters, the main novelty of our procedure is the extraction of the evolution of the trapped charge density of these two traps with time (Figs. 3(c), 4(b), 5(b)–5(d)), which modify the values of V_T (12) (Figs. 3(d), 4(c), 5(e)) and V_{SS} (13) (Figs. 3(e), 4(d), 5(f)).

The time evolution of V_T during the transfer characteristic sweep, extracted from our procedure, is shown in Fig. 4(c). Its value varies from the initial value $V_{T_t} = -3.37$ V (x_4) and a minimum value of -9.4 V, near the end of the voltage sweep. This range of values of $V_T(t)$ agrees with the position of the knee in the logarithmic $I_D{-}V_G$ curves of Fig. 4(a), in which the slope of these curves changes from exponential to quadratic. The detected net threshold voltage shift is around 6 V, which is in good agreement with the 6 V shift of the experimental transfer curves shown in Fig. 4(a).

The range in which V_T varies during the $I_D{-}V_D$ experiment is seen in Fig. 3(d). This range is larger and different than the one seen in Fig. 4(c) for the $I_D - V_G$ curves. This is due to the different duration of these two experiments, the former being much longer than the later; and due to the different initialization routines ($V_G(t = 0) = -20$ V for the $I_D{-}V_D$ experiment and $V_G(t = 0) = +20$ V for the $I_D{-}V_G$ experiment). Note also that the drain current at $V_G = -80$ V and $V_D = -80$ V is greater in the $I_D - V_G$ experiment (Fig. 4(a)) than in the $I_D - V_D$ one (Fig. 3(a)). This can be explained with more negative values for V_T in the $I_D - V_D$ experiment, thus, reducing the drain current. The drain current in the $I_D - V_D$ experiment for $V_G = -60$ and -40 V is reduced from OFF-to-ON (Fig. 3(a)) to ON-to-OFF (Fig. 3(b)), which justifies the change of V_T to more negative values (Fig. 3(d))

The variation of V_T depicted in Figs. 3(d) and 4(c) is related to the time evolution of the trapped charge density $Q_{tL}(t)$ during the $I_D - V_D$ and $I_D - V_G$ experiments (Figs. 3(c) and 4(b), respectively). This trapped-charge variation corresponds to trap #1. In the $I_D - V_G$ experiment, its value changes from the initial value $Q_{tL}(0) = 0$ C/cm^2, since the transistor is in deep sub-threshold region, with no holes available to be trapped, up to a maximum value of 6.8×10^{-8} C/cm^2, near the end of the voltage sweep. This is equivalent to a variation in the occupied traps of 4.2×10^{11} cm^{-2} during the 4 s experiment. In the $I_D - V_D$ experiment, the value of the initial trapped charge is not zero because $V_G = -20$ V and holes from the channel are trapped during the first 3 s prior to sweeping V_D. The extracted initial value is 3.23×10^{-7} C/cm^2 (or 2.01×10^{-12} cm^{-2} initially occupied traps). It reaches a maximum of 5.21×10^{-7} C/cm^2 (or 3.25×10^{12} cm^{-2} occupied traps). The mean variation of the trapped charge during any of the six single combined forward–backward $I_D - V_D$ scans of 3.2 s is around 0.9×10^{-7} C/cm^2 (or 5.7×10^{11} cm^{-2} variation of occupied traps). The maximum variation of trapped charge #1 during the first 5 s of the current transient $I_D - t$ (red curve in Fig. 5(c)) is 0.8×10^{-8} C/cm^2 (or a maximum variation in the occupied trap #1 of 0.5×10^{11} cm^{-2}). The variation in the occupied-trap density for trap #1 during the first 5 s of the red $I_D - t$ experiment in Fig. 5(c) is lower but consistent with the variations observed in the other two experiments (Figs. 3(c) and 4(b)) during similar time intervals. These differences can be explained by the different measurement protocols (Fig. S2).

As mentioned above, trap #2 is detected only in the $I_D{-}t$ transients due to its large time constant. The variation of the occupied-trap

Table 1
Extracted values of the parameters composing the individual representation x. Checked boxes indicate the experiment is aimed to fit. μ_0 is in cm^2/Vs, α_s is in A/V$^{2+\gamma}$, $Q_{tL,1}$ is in C/cm^2, τ_1 and τ_2 are in s, V_T is in V and V_{SS} is in V.

x	Value	Fitting		
(Parameters)		$I_D - V_D$	$I_D - V_G$	$I_D - t$
$x_1 = \mu_0$	1.31	☒	☒	☒
$x_2 = \gamma$	1.14×10^{-13}	☒	☒	☒
$x_3 = V_{T_o}$	−15	☒	☐	☐
$x_4 = V_{T_t}$	−3.37	☐	☒	☒
$x_5 = V_{SS_o}$	14.37	☒	☐	☐
$x_6 = V_{SS_t}$	3.62	☐	☒	☒
$x_7 = \alpha_s$	1.93×10^{-08}	☒	☒	☒
$x_8 = \beta_{1_{o,f}}$	9.45×10^{-04}	☒	☐	☐
$x_9 = \beta_{1_{o,b}}$	-9.81×10^{-04}	☒	☐	☐
$x_{10} = \beta_{1_{t,f}}$	-3.93×10^{-04}	☐	☒	☒
$x_{11} = \beta_{1_{t,b}}$	-1.55×10^{-03}	☐	☒	☐
$x_{12} = \beta_{2_{t,f}}$	-3.73×10^{-05}	☐	☐	☒
$x_{13} = m_s$	0.98	☒	☒	☒
$x_{14} = s$	8.32	☒	☒	☒
$x_{15} = \tau_1$	13.23	☒	☒	☒
$x_{16} = \tau_2$	1000	☐	☐	☒
$x_{17} = Q_{tL,1}$	3.23×10^{-07}	☒	☐	☐
$x_{18} = 1/\lambda$	$\lambda = 0$	☒	☒	☒

density for this second trap (Fig. 5(d)) is almost one order of magnitude larger than the variation of the first trap (Fig. 5(c)). It means that the concentration of trap #2 is larger than trap #1; and trap #2 is mainly responsible for the long term device behavior.

One interesting point that can be extracted from the fitting is the sharp increase with rebound of the current seen in Fig. 3(a) at $V_D = -80$ V in the two upper curves ($V_G = -60$ and -80 V), just when the backward sweeps begin. This phenomenon was also observed in the experimental data looking closely at this point in ([50], Fig. 4). The authors explained the increment of the current because at constant V_G, when V_D is more negative, trapped holes are released and the trapped charge density decreases ([50], see also Figs. 2 and 6). Thus, the higher number of available charge carriers increases the drain current in the backward sweep of the output characteristics. At the same time, the drain current tends to decrease when V_D starts decreasing in the backward sweep. This produces the above-mentioned rebound. The decrease of the trapped charge density when V_D is more negative, including a rebound for the curves at $V_G = -60$ and -80 V, is reproduced in our simulations (Fig. 3(c)).

Another interesting point in Fig. 3 is that the drain current in curves $V_G = -60$ and -40 V in Fig. 3(b) is lower than in Fig. 3(a). A lower current is explained by a lower number of available free holes or a higher number of trapped holes. This is reproduced with our simulations in Fig. 3(c): the trapped charge density for the cases $V_G = -60$ and -40 V is higher in the red-green curves than in the black-blue ones. The value of the charge density is comparable to that of the $V_G = -80$ V curve because the trapped charges react more slowly than the voltage scan.

6. Conclusions

A semi-empirical model that describes the evolution of the threshold voltage and trapped charge density in OTFTs under dynamic conditions was developed. It was expressed as a continuity equation for the trapped charges in the transistor, including two main terms: a generation-like term proportional to the drain current and a recombination term controlled by a time constant. It was included in a compact model that evaluates the drain current in the transistor. The resulting model was combined with an evolutionary parameter extraction procedure.

The procedure was tested in the experimental output and transfer characteristics with hysteresis and current transients measured in pentacene-based transistors. The procedure extracts the parameters of the transistor model. Our calculations reproduce faithfully three different kinds of experiments at the same time, as well as provides information about the evolution of the trapped charge and threshold voltage over all measurements. The complete evolution of the trapped charge and threshold voltage is a step forward in the understanding of phenomena that take place in transistors with hysteresis.

One of the issues that require further investigation is to gain physical insight on the parameters that control the continuity equation for the trapped charges in the transistor, in particular on the proportional constant β that multiplies the drain current in this equation, since different values of this parameter were required to fit different experiments. Most probably, this parameter should take into account the trap distribution, thus being dependent not only on the current, but also on the already trapped charge and the applied voltages. In this regard, being able to model the behavior of this parameter would allow decision makers to extract more reliable and higher quality information on the impact of hysteresis on OTFTs.

CRediT authorship contribution statement

A. Romero: Writing – original draft, Visualization, Validation, Software, Investigation, Data curation. **J.A. Jiménez-Tejada:** Writing – review & editing, Writing – original draft, Validation, Supervision, Project administration, Methodology, Investigation, Conceptualization. **R. Picos:** Writing – review & editing, Data curation, Conceptualization. **D. Lara:** Validation, Software, Data curation. **J.B. Roldán:** Writing – review & editing, Funding acquisition, Formal analysis, Conceptualization. **M.J. Deen:** Writing – review & editing, Validation, Investigation.

Declaration of competing interest

The authors declare that they have no known competing financial interests or personal relationships that could have appeared to influence the work reported in this paper.

Data availability

The model formula and data extraction code can be found in the supplementary material.

Appendix A. Justification of the model

Consider an electron (or hole) deep trap distributed uniformly in the semiconductor of an N-type (P-type) Thin Film Transistor (TFT) with a concentration per unit volume N_T. In the following, we refer only to electrons and electron traps in a N-type TFT, although the study can also be applied indistinctly to holes and hole traps in a P-type TFT. The concentration per unit volume of occupied traps is n_T, c_n is the electron capture coefficient, e_n is the electron emission coefficient, and n is the electron density. The net rate of occupied deep traps is given by

$$\frac{dn_T}{dt} = c_n n(N_T - n_T) - e_n n_T. \tag{A.1}$$

If this deep trap is located in the intrinsic n-channel of a TFT, in which a large concentration of free charge electrons exists and $c_n n \gg e_n$, then (A.1) can be reduced to

$$\frac{dn_T}{dt} \approx c_n n(N_T - n_T). \tag{A.2}$$

Consider a section of this TFT of length dx with a semiconductor layer of thickness y_{max} (Fig. 6). For a gate voltage V_G, the free charge carriers are located at the bottom of the semiconductor channel in the region $[0, y_G = y_G(V_G)]$. The traps are able to be filled in the range $[0, y_G]$ in which free charge carriers are available, and are empty elsewhere.

Integrating (A.2) in the range $[0, y_{max}]$, different definitions of densities per unit area can be obtained:

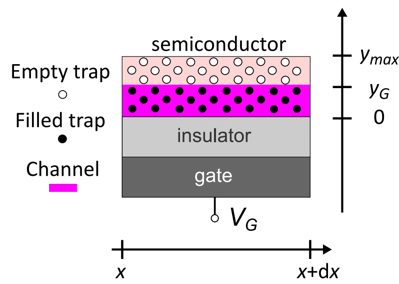

Fig. 6. Section of the TFT channel with occupied and empty traps.

Free charge density per unit area.

$$Q_x = q\int_0^{y_{max}} n\mathrm{d}y = q\int_0^{y_G} n\mathrm{d}y + \underbrace{q\int_{y_G}^{y_{max}} n\mathrm{d}y}_{0} = q\int_0^{y_G} n\mathrm{d}y, \tag{A.3}$$

where q is the charge of the free carrier, and $n = 0$ in $[y_G, y_{max}]$ because the free charges are available only in $[0, y_G]$.

Concentration of occupied traps per unit area.

$$n_t = \int_0^{y_{max}} n_T\mathrm{d}y = \int_0^{y_G} n_T\mathrm{d}y + \underbrace{\int_{y_G}^{y_{max}} n_T\mathrm{d}y}_{0} = \int_0^{y_G} n_T\mathrm{d}y, \tag{A.4}$$

where $n_T = 0$ in $[y_G, y_{max}]$ because the absence of free charge carriers means that the traps are not charged.

Trapped charge density per unit area.

$$Q_t = qn_t \tag{A.5}$$

Mean value of the trapped charge density.

$$Q_{tL} = \frac{1}{L}\int_0^L Q_t\mathrm{d}x \tag{A.6}$$

Once the previous concepts have been introduced, two completely different scenarios are presented for relation (A.2) in the semiconductor of a TFT, as can be seen in Fig. 2.

(i) $V_D = 0\,\mathrm{V}$, and thus, the drain current $I_D = 0\,\mathrm{A}$ (Fig. 2(a)). The free charges are confined in a layer of thickness y_G uniformly distributed along the channel length L of the transistor. The distribution of trapped charges is also uniform. Integrating (A.2) in the range $[0, y_{max}]$ results:

$$\int_0^{y_{max}} \frac{\mathrm{d}n_T}{\mathrm{d}t}\mathrm{d}y \approx \int_0^{y_{max}} c_n N_T\mathrm{d}y - \int_0^{y_{max}} c_n n n_T\mathrm{d}y, \tag{A.7}$$

$$\frac{\mathrm{d}n_t}{\mathrm{d}t} \approx \int_0^{y_G} c_n n N_T\mathrm{d}y - \int_0^{y_G} c_n n n_T\mathrm{d}y. \tag{A.8}$$

Assuming that the free charge carriers thermalize quicker than the trapped charge, a time constant can be defined as $\tau = 1/(c_n n)$. Then, (A.8) multiplied by q can be written as:

$$q\frac{\mathrm{d}n_t}{\mathrm{d}t} \approx \frac{qN_T y_G}{\tau} - \frac{qn_t}{\tau}, \tag{A.9}$$

$$\frac{\mathrm{d}Q_t}{\mathrm{d}t} \approx \frac{Q_{t0}}{\tau} - \frac{Q_t}{\tau}, \tag{A.10}$$

where $Q_{t0} = Q_{t0}(V_G) = qN_T y_G$. This equation means that variations in the trapped charge are produced only by changes in V_G. Once V_G changes, the trapped charge evolves to a new steady state, $Q_t(t\to\infty) = qN_T y_G$, at a rate controlled by the time constant τ.

Integrating (A.10) along the channel length L and using (A.6) results in:

$$\frac{\mathrm{d}Q_{tL}}{\mathrm{d}t} \approx \frac{Q_{t0}}{\tau} - \frac{Q_{tL}}{\tau}, \tag{A.11}$$

which coincides with (14) in the main text.

(ii) $V_D \neq 0$ and $I_D \neq 0$ (Fig. 2(b)). The distributions of free and trapped charges are not uniform across the channel length L of the transistor. Variations in the trapped charge are produced by changes in the gate or drain voltages bringing the transistor into a new steady state. In this case, the integration of (A.2) shown in (A.8), is treated in a different way. In order to take into account the non-uniformity of the distribution of free charge carriers along the channel and the flow of these free charges through the channel, (A.8) is transformed into:

$$\frac{\mathrm{d}(qn_t)}{\mathrm{d}t} \approx c_n N_T \int_0^{y_G} qn\mathrm{d}y - \int_0^{y_G} \frac{qn_T}{\tau}\mathrm{d}y, \tag{A.12}$$

$$\frac{\mathrm{d}Q_t}{\mathrm{d}t} \approx c_n N_T Q_x - \frac{Q_t}{\tau}, \tag{A.13}$$

in which definitions (A.3)–(A.5) have been introduced.

Integrating (A.13) along the channel length L and using (A.6) results:

$$\frac{\mathrm{d}Q_{tL}}{\mathrm{d}t} = \frac{N_T c_n}{L}\int_0^L Q_x dx - \frac{Q_{tL}}{\tau}. \tag{A.14}$$

Taking the expression for the current per unit width [46]

$$\frac{I_D}{W} = Q_x \mu_x |E_x|, \tag{A.15}$$

and introducing it into (A.14), the next relation is obtained:

$$\frac{\mathrm{d}Q_{tL}}{\mathrm{d}t} = \frac{N_T c_n I_D}{LW}\int_0^L \frac{1}{\mu_x|E_x|}\mathrm{d}x - \frac{Q_{tL}}{\tau}. \tag{A.16}$$

Now, defining β as

$$\beta = \frac{N_T c_n}{LW}\int_0^L \frac{1}{\mu_x|E_x|}dx, \tag{A.17}$$

relation (A.14) can be written as:

$$\frac{\mathrm{d}Q_{tL}}{\mathrm{d}t} = \beta I_D - \frac{Q_{tL}}{\tau}, \tag{A.18}$$

which is the same as (16) in the main text. Note that β can be seen as a proportionality constant that modulates I_D.

Appendix B. Supplementary data

Supplementary material related to this article can be found online at https://doi.org/10.1016/j.orgel.2024.107048.

References

[1] J.Y. Oh, S. Rondeau-Gagné, Y.-C. Chiu, A. Chortos, F. Lissel, G.-J.N. Wang, B.C. Schroeder, T. Kurosawa, J. Lopez, T. Katsumata, J. Xu, C. Zhu, X. Gu, W.-G. Bae, Y. Kim, L. Jin, J.W. Chung, J.B.-H. Tok, Z. Bao, Intrinsically stretchable and healable semiconducting polymer for organic transistors, Nature 539 (7629) (2016) 411–415.
[2] J. Xu, S. Wang, G.-J.N. Wang, C. Zhu, S. Luo, L. Jin, X. Gu, S. Chen, V.R. Feig, J.W.F. To, S. Rondeau-Gagné, J. Park, B.C. Schroeder, C. Lu, J.Y. Oh, Y. Wang, Y.-H. Kim, H. Yan, R. Sinclair, D. Zhou, G. Xue, B. Murmann, C. Linder, W. Cai, J.B.-H. Tok, J.W. Chung, Z. Bao, Highly stretchable polymer semiconductor films through the nanoconfinement effect, Science 355 (6320) (2017) 59–64.
[3] J.Y. Oh, D. Son, T. Katsumata, Y. Lee, Y. Kim, J. Lopez, H.-C. Wu, J. Kang, J. Park, X. Gu, J. Mun, N.G.-J. Wang, Y. Yin, W. Cai, Y. Yun, J.B.-H. Tok, Z. Bao, Stretchable self-healable semiconducting polymer film for active-matrix strain-sensing array, Sci. Adv. 5 (11) (2019) 1–9.
[4] S. Wang, J. Xu, W. Wang, G.-J.N. Wang, R. Rastak, F. Molina-Lopez, J.W. Chung, S. Niu, V.R. Feig, J. Lopez, T. Lei, S.-K. Kwon, Y. Kim, A.M. Foudeh, A. Ehrlich, A. Gasperini, Y. Yun, B. Murmann, J.B.-H. Tok, Z. Bao, Skin electronics from scalable fabrication of an intrinsically stretchable transistor array, Nature 555 (7694) (2018) 83–88.
[5] W. Wu, H. Zhang, Y. Wang, S. Ye, Y. Guo, C. Di, G. Yu, D. Zhu, Y. Liu, High-performance organic transistor memory elements with steep flanks of hysteresis, Adv. Funct. Mater. 18 (17) (2008) 2593–2601.
[6] M.J. Deen, M.H. Kazemeini, Y.M. Haddara, J. Yu, G. Vamvounis, S. Holdcroft, W. Woods, Electrical characterization of polymer-based FETs fabricated by spin-coating poly(3-alkylthiophene)s, IEEE Trans. Electron. Devices 51 (11) (2004) 1892–1901.
[7] O. Marinov, M. Deen, B. Iniguez, Charge transport in organic and polymer thin-film transistors: recent issues, IEE Proc.-Circuits Devices Syst. 152 (3) (2005) 189.

[8] M. Ba, S. Mansouri, A. Jouili, Y. Yousfi, L. Chouiref, M. Jdir, M. Erouel, F. Yakuphanoglu, L.E. Mir, Controlling of hysteresis by varying ZnO-nanoparticles amount in P3HT:Zno hybrid thin-film transistor: Modeling, J. Electron. Mater. 52 (2) (2022) 1203–1215.
[9] Y. Hu, L. Zheng, J. Li, Y. Huang, Z. Wang, X. Lu, L. Yu, S. Wang, Y. Sun, S. Ding, D. Ji, Y. Lei, X. Chen, L. Li, W. Hu, Organic phase-change memory transistor based on an organic semiconductor with reversible molecular conformation transition, Adv. Sci. 10 (4) (2022) 2205694.
[10] S. Lee, H. Seong, S.G. Im, H. Moon, S. Yoo, Organic flash memory on various flexible substrates for foldable and disposable electronics, Nature Commun. 8 (1) (2017) 1–9.
[11] J.H. Park, S.A. Khan, M.K. Rahmani, J. Cho, M.H. Kang, Enhancement of resistive switching behavior of organic resistive random access memory devices through UV-ozone treatment, Mater. Res. Express 9 (8) (2022) 085903.
[12] B. Mu, H.-H. Hsu, C.-C. Kuo, S.-T. Han, Y. Zhou, Organic small molecule-based RRAM for data storage and neuromorphic computing, J. Mater. Chem. C 8 (37) (2020) 12714–12738.
[13] S. Pathania, J.J.L. Hmar, V. Kumar, P. Chinnamuthu, Advances in flexible non-volatile resistive switching memory based on organic poly (3, 4-ethylenedioxythio phene): Poly (styrenesulfonate) film, Thin Solid Films 763 (2022) 139605.
[14] K.-J. Lee, T.-Y. Yang, D.-W. Chou, Y.-H. Wang, Hybrid ferroelectric p(VDF-TrFE)/BZT insulators for pentacene-based nonvolatile memory applications, IEEE Electron Device Lett. 43 (9) (2022) 1463–1466.
[15] A.A. Boampong, J.-H. Cho, Y. Choi, M.-H. Kim, Solution-processed dual gate ferroelectric–ferroelectric organic polymer field-effect transistor for the multibit nonvolatile memory, Adv. Electron. Mater. 7 (10) (2021) 2100430.
[16] M. Xu, W. Qi, W. Xie, W. Wang, High-speed, low-voltage programmable/erasable flexible 2-bit organic transistor nonvolatile memory with a monolayer buffered ferroelectric terpolymer insulator, Appl. Phys. Lett. 121 (8) (2022) 083502.
[17] S. He, M. Guo, Y. Wang, Y. Liang, Y. Shen, An optical/ferroelectric multiplexing multidimensional nonvolatile memory from ferroelectric polymer, Adv. Mater. 34 (24) (2022) 2202181.
[18] I.S. Zlobin, Y.V. Nelyubina, V.V. Novikov, Molecular compounds in spintronic devices: An intricate marriage of chemistry and physics, Inorg. Chem. 61 (33) (2022) 12919–12930.
[19] M. Deen, O. Marinov, S. Holdcroft, W. Woods, Low-frequency noise in polymer transistors, IEEE Trans. Electron. Devices 48 (8) (2001) 1688–1695.
[20] O. Marinov, M.J. Deen, J.A. Jiménez-Tejada, Low-frequency noise in downscaled silicon transistors: Trends, theory and practice, Phys. Rep. 990 (2022) 1–179.
[21] O. Marinov, M. Deen, J. Jiménez-Tejada, C. Chen, Variable-range hopping charge transport in organic thin-film transistors, Phys. Rep. 844 (2020) 1–105.
[22] M. Deen, M. Kazemeini, Photosensitive polymer thin-film FETs based on poly(3-octylthiophene), Proc. IEEE 93 (7) (2005) 1312–1320.
[23] D.I. Kim, N.Y. Kwon, S. hun Lee, M.J. Cho, J. Kim, D.H. Choi, J. Joo, High hysteresis and distinctive optoelectronic memory effect for ambipolar thin-film transistors using a conjugated polymer having donor-acceptor heterojunction, Org. Electron. 108 (2022) 106599.
[24] S. Dutta, K.S. Narayan, Gate-voltage control of optically-induced charges and memory effects in polymer field-effect transistors, Adv. Mater. 16 (23–24) (2004) 2151–2155.
[25] A. Li, X. Wei, Y. He, C. He, M.U. Ali, H. Yang, O. Goto, H. Meng, Traps induced memory effect in rubrene single crystal phototransistor, Appl. Phys. Lett. 113 (10) (2018) 103301.
[26] A. Jaafar, M. Al Chawa, F. Cheng, S. Kelly, R. Picos, R. Tetzlaff, N. Kemp, Polymer/TiO_2 nanorod nanocomposite optical memristor device, J. Phys. Chem. C 125 (27) (2021) 14965–14973.
[27] J. Lee, S. Pak, Y.-W. Lee, Y. Cho, J. Hong, P. Giraud, H.S. Shin, S.M. Morris, J.I. Sohn, S. Cha, J.M. Kim, Monolayer optical memory cells based on artificial trap-mediated charge storage and release, Nature Commun. 8 (1) (2017) 1–8.
[28] X. Zhao, Z. Wang, H. Xu, Y. Liu, Two-terminal optoelectronic memory device, in: Photo-Electroactive Nonvolatile Memories for Data Storage and Neuromorphic Computing, Elsevier, 2020, pp. 75–105.
[29] D.K. Hwang, M.S. Oh, J.M. Hwang, J.H. Kim, S. Im, Hysteresis mechanisms of pentacene thin-film transistors with polymer/oxide bilayer gate dielectrics, Appl. Phys. Lett. 92 (1) (2008) 013304.
[30] G. Gu, M.G. Kane, J.E. Doty, A.H. Firester, Electron traps and hysteresis in pentacene-based organic thin-film transistors, Appl. Phys. Lett. 87 (24) (2005) 243512.
[31] Y. Hernandez-Barrios, F. Avila, M. Estrada, A. Cerdeira, O. Moldovan, B. Iñiguez, R. Picos, Modeling the variation of threshold voltage, mobility factor and saturation coefficient in amorphous indium-gallium-zinc oxide thin film transistors, in: 2016 13th International Conference on Electrical Engineering, Computing Science and Automatic Control, CCE, IEEE, 2016, pp. 1–4.
[32] S. Chae, T.I. Lee, J.Y. Oh, Reduced electrical hysteresis of organic thin-film transistors based on small molecule semiconductor through an insulating polymer binder, Korean J. Chem. Eng. 39 (3) (2022) 499–503.
[33] X. Su, X. Wu, S. Chen, A.M. Nedumaran, M. Stephen, K. Hou, B. Czarny, W.L. Leong, A highly conducting polymer for self-healable, printable, and stretchable organic electrochemical transistor arrays and near hysteresis-free soft tactile sensors, Adv. Mater. 34 (19) (2022) 2200682.
[34] H. Bai, Y. Yang, R.M. Voyles, R.A. Nawrocki, A no-hysteresis TIPS–pentacene:polystyrene blend-based organic field effect transistor by extruded direct ink writing and the application in a resistive load inverter circuit, J. Mater. Chem. C 10 (30) (2022) 10973–10980.
[35] Y. Xu, C. Liu, D. Khim, Y.-Y. Noh, Development of high-performance printed organic field-effect transistors and integrated circuits, Phys. Chem. Chem. Phys. 17 (40) (2015) 26553–26574.
[36] Z.A. Lamport, H.F. Haneef, S. Anand, M. Waldrip, O.D. Jurchescu, Tutorial: Organic field-effect transistors: Materials, structure and operation, J. Appl. Phys. 124 (7) (2018) 071101.
[37] R. Picos, E. Garcia-Moreno, M.M. Al Chawa, L.O. Chua, Using memristor formalism in semiconductor device modeling, in: Electrochemical Society Meeting Abstracts 231, no. 45, The Electrochemical Society, Inc., 2017, 2048–2048.
[38] K.M. Awawdeh, J.A. Jiménez-Tejada, P. López-Varo, J.A. López-Villanueva, F.M. Gómez-Campos, M.J. Deen, Characterization of organic thin film transistors with hysteresis and contact effects, Org. Electron. 14 (12) (2013) 3286–3296.
[39] W.L. Kalb, F. Meier, K. Mattenberger, B. Batlogg, Defect healing at room temperature in pentacene thin films and improved transistor performance, Phys. Rev. B 76 (18) (2007) 184112.
[40] W.L. Kalb, B. Batlogg, Calculating the trap density of states in organic field-effect transistors from experiment: A comparison of different methods, Phys. Rev. B 81 (3) (2010) 035327.
[41] S. Jung, J.W. Jin, V. Mosser, Y. Bonnassieux, G. Horowitz, A compact model and parameter extraction method for a staggered OFET with power-law contact resistance and mobility, IEEE Trans. Electron Devices 66 (11) (2019) 4894–4900.
[42] C.H. Kim, A. Castro-Carranza, M. Estrada, A. Cerdeira, Y. Bonnassieux, G. Horowitz, B. Iniguez, A compact model for organic field-effect transistors with improved output asymptotic behaviors, IEEE Trans. Electron. Devices 60 (3) (2013) 1136–1141.
[43] F. Torricelli, M. Ghittorelli, M. Rapisarda, A. Valletta, L. Mariucci, S. Jacob, R. Coppard, E. Cantatore, Z.M. Kovács-Vajna, L. Colalongo, Unified drain-current model of complementary p- and n-type OTFTs, Org. Electron. 22 (2015) 5–11.
[44] F. Hain, M. Graef, B. Iñiguez, A. Kloes, Charge based, continuous compact model for the channel current in organic thin-film transistors for all regions of operation, Solid-State Electron. 133 (2017) 17–24.
[45] J. Pruefer, J. Leise, G. Darbandy, A. Nikolaou, H. Klauk, J.W. Borchert, B. Iniguez, T. Gneiting, A. Kloes, Compact modeling of short-channel effects in staggered organic thin-film transistors, IEEE Trans. Electron. Devices 67 (11) (2020) 5082–5090.
[46] O. Marinov, M.J. Deen, U. Zschieschang, H. Klauk, Organic thin-film transistors: Part I-Compact DC modeling, IEEE Trans. Electron Devices 56 (12) (2009) 2952–2961.
[47] J.A. Jiménez-Tejada, J.A. López-Villanueva, P. López-Varo, K.M. Awawdeh, M.J. Deen, Compact modeling and contact effects in organic transistors, IEEE Trans. Electron Devices 61 (2) (2014) 266–277.
[48] A. Romero, J. González, M. Deen, J.A. Jiménez-Tejada, Versatile model for the contact region of organic thin-film transistors, Org. Electron. 77 (2020) 105523.
[49] A. Romero, J. Jiménez-Tejada, J. González, M. Deen, Unified electrical model for the contact regions of staggered thin film transistors, Org. Electron. 92 (2021) 106129.
[50] C. Ucurum, H. Goebel, F.A. Yildirim, W. Bauhofer, W. Krautschneider, Hole trap related hysteresis in pentacene field-effect transistors, J. Appl. Phys. 104 (8) (2008) 084501.
[51] M.J. Deen, O. Marinov, U. Zschieschang, H. Klauk, Organic thin-film transistors: Part II. Parameter extraction, IEEE Trans. Electron Devices 56 (12) (2009) 2962–2968.
[52] M. Fayez, K.M. Morsi, M.N. Sabry, OTFTs compact models: analysis, comparison, and insights, IET Circuits Device Syst. 11 (5) (2017) 409–420.
[53] A. Romero, J. González, R. Picos, M.J. Deen, J.A. Jiménez-Tejada, Evolutionary parameter extraction for an organic TFT compact model including contact effects, Org. Electron. 61 (2018) 242–253.
[54] A. Romero, C. Jiménez, J. González, P. López-Varo, M.J. Deen, J.A. Jiménez-Tejada, Compact modeling of the effects of illumination on the contact region of organic phototransistors, Org. Electron. 70 (2019) 113–121.
[55] S. Abdinia, F. Torricelli, G. Maiellaro, R. Coppard, A. Daami, S. Jacob, L. Mariucci, G. Palmisano, E. Ragonese, F. Tramontana, A. van Roermund, E. Cantatore, Variation-based design of an AM demodulator in a printed complementary organic technology, Org. Electron. 15 (4) (2014) 904–912.
[56] A. Valletta, M. Rapisarda, S. Calvi, G. Fortunato, M. Frasca, G. Maira, A. Ciccazzo, L. Mariucci, A DC and small signal AC model for organic thin film transistors including contact effects and non quasi static regime, Org. Electron. 41 (Supplement C) (2017) 345–354.
[57] A.M. Ma, D.W. Barlage, Analysis of the channel and contact regions in staggered and drain-offset ZnO thin-film transistors with compact modeling, IEEE Trans. Electron Devices 65 (8) (2018) 3277–3282.
[58] R. Martins, D. Gaspar, M.J. Mendes, L. Pereira, J. Martins, P. Bahubalindruni, P. Barquinha, E. Fortunato, Papertronics: Multigate paper transistor for multifunction applications, Appl. Mater. Today 12 (2018) 402–414.

[59] M. Buonomo, N. Lago, G. Cantarella, N. Wrachien, M. Natali, F. Prescimone, E. Benvenuti, M. Muccini, S. Toffanin, A. Cester, Simple and accurate single transistor technique for parameters extraction from organic and inorganic thin film devices, Org. Electron. 63 (2018) 376–383.
[60] S. Fatima, U. Rafique, U. Ahmed, M. Ahmed, A global parameters extraction technique to model organic field effect transistors output characteristics, Solid-State Electron. 152 (2019) 81–92.
[61] O. Marinov, M.J. Deen, R. Datars, Compact modeling of charge carrier mobility in organic thin-film transistors, J. Appl. Phys. 106 (6) (2009) 064501.
[62] L. Bürgi, T.J. Richards, R.H. Friend, H. Sirringhaus, Close look at charge carrier injection in polymer field-effect transistors, J. Appl. Phys. 94 (9) (2003) 6129–6137.
[63] A. Valletta, A. Daami, M. Benwadih, R. Coppard, G. Fortunato, M. Rapisarda, F. Torricelli, L. Mariucci, Contact effects in high performance fully printed p-channel organic thin film transistors, Appl. Phys. Lett. 99 (23) (2011) 233309.
[64] L. Mariucci, M. Rapisarda, A. Valletta, S. Jacob, M. Benwadih, G. Fortunato, Current spreading effects in fully printed p-channel organic thin film transistors with Schottky source–drain contacts, Org. Electron. 14 (1) (2013) 86–93.
[65] M. Charbonneau, D. Locatelli, S. Lombard, C. Serbutoviez, L. Tournon, F. Torricelli, S. Abdinia, E. Cantatore, M. Fattori, A large-area gravure printed process for P-type organic thin-film transistors on plastic substrates, in: 2018 48th European Solid-State Device Research Conference, ESSDERC, IEEE, 2018, pp. 70–73.
[66] J.A. Jiménez-Tejada, K.M. Awawdeh, J.A. López-Villanueva, J.E. Carceller, M.J. Deen, N.B. Chaure, T. Basova, A.K. Ray, Contact effects in compact models of organic thin film transistors: Application to zinc phthalocyanine-based transistors, Org. Electron. 12 (5) (2011) 832–842.
[67] J.A. Jiménez-Tejada, P. López-Varo, A.N. Cammidge, I. Chambrier, M.J. Cook, N.B. Chaure, A.K. Ray, Compact modeling of organic thin-film transistors with solution processed octadecyl substituted tetrabenzotriazaporphyrin as an active layer, IEEE Trans. Electron Devices 64 (6) (2017) 2629–2634.
[68] J.A. Jiménez-Tejada, P. Lopez-Varo, N.B. Chaure, I. Chambrier, A.N. Cammidge, M.J. Cook, A. Jafari-Fini, A.K. Ray, Organic thin film transistors using a liquid crystalline palladium phthalocyanine as active layer, J. Appl. Phys. 123 (11) (2018) 115501.
[69] T.J. Richards, H. Sirringhaus, Analysis of the contact resistance in staggered, top-gate organic field-effect transistors, J. Appl. Phys. 102 (9) (2007) 094510.
[70] C.W. Sohn, T.U. Rim, G.B. Choi, Y.H. Jeong, Analysis of contact effects in inverted-staggered organic thin-film transistors based on anisotropic conduction, IEEE Trans. Electron Devices 57 (5) (2010) 986–994.
[71] F.V. Di Girolamo, C. Aruta, M. Barra, P. D'Angelo, A. Cassinese, Organic film thickness influence on the bias stress instability in sexithiophene field effect transistors, Appl. Phys. A 96 (2) (2009) 481–487.
[72] S. Zafar, A. Callegari, E. Gusev, M.V. Fischetti, Charge trapping related threshold voltage instabilities in high permittivity gate dielectric stacks, J. Appl. Phys. 93 (11) (2003) 9298–9303.
[73] K.P. Pernstich, S. Haas, D. Oberhoff, C. Goldmann, D.J. Gundlach, B. Batlogg, A.N. Rashid, G. Schitter, Threshold voltage shift in organic field effect transistors by dipole monolayers on the gate insulator, J. Appl. Phys. 96 (11) (2004) 6431–6438.
[74] M. Sze, K.K. Ng, Physics of Semiconductor Devices, Wiley, 2006.
[75] A. Rolland, J. Richard, J.P. Kleider, D. Mencaraglia, Electrical properties of amorphous silicon transistors and MIS-devices: Comparative study of top nitride and bottom nitride configurations, J. Electrochem. Soc. 140 (12) (1993) 3679–3683.
[76] M. McDowell, I.G. Hill, J.E. McDermott, S.L. Bernasek, J. Schwartz, Improved organic thin-film transistor performance using novel self-assembled monolayers, Appl. Phys. Lett. 88 (7) (2006) 073505.
[77] M.-H. Yoon, C. Kim, A. Facchetti, T.J. Marks, Gate dielectric chemical structure-organic field-effect transistor performance correlations for electron, hole, and ambipolar organic semiconductors, J. Am. Chem. Soc. 128 (39) (2006) 12851–12869.
[78] H.-C. Lin, C.-H. Hung, W.-C. Chen, Z.-M. Lin, H.-H. Hsu, T.-Y. Hunag, Origin of hysteresis in current-voltage characteristics of polycrystalline silicon thin-film transistors, J. Appl. Phys. 105 (5) (2009) 054502.
[79] C. Ucurum, Understanding and Modeling the Hysteresis in Current-Voltage (I–V) and Capacitance-Voltage (C–V) Characteristics of Organic Thin-Film Transistors (Ph.D. thesis), Fakultät für Elektrotechnik der Helmut-Schmidt-Universität/Universität der Bundeswehr Hamburg, 2013.
[80] R. Picos, M. Roca, B. Iñiguez, E. García-Moreno, A new MOSFET parameter extraction method using genetic algorithms, in: Conferencia Dispositivos Electrónicos (CDE) 1999, 1999.
[81] P. Moreno, R. Picos, M. Roca, E. Garcia-Moreno, B. Iniguez, M. Estrada, Parameter extraction method using genetic algorithms for an improved OTFT compact model, in: 2007 Spanish Conference on Electron Devices, IEEE, 2007, pp. 64–67.
[82] A. Romero, J. González, J.A. Jiménez-Tejada, Constrained many-objective evolutionary extraction procedure for an OTFT compact model including contact effects, in: 2018 Spanish Conference on Electron Devices, CDE, IEEE, 2018, pp. 1–4.
[83] R.L. Burden, D.J. Faires, Numerical Analysis, third ed., PWS Publishing Company, Boston, 1985.
[84] J. González, I. Rojas, J. Ortega, H. Pomares, F. Fernandez, A. Díaz, Multiobjective evolutionary optimization of the size, shape, and position parameters of radial basis function networks for function approximation, IEEE Trans. Neural Netw. 14 (6) (2003) 1478–1495.
[85] A. Cerdeira, M. Estrada, R. García, A. Ortiz-Conde, F.G. Sánchez, New procedure for the extraction of basic a-Si:H TFT model parameters in the linear and saturation regions, Solid-State Electron. 45 (7) (2001) 1077–1080.
[86] J.A. Jiménez-Tejada, A. Romero, J. González, N.B. Chaure, A.N. Cammidge, I. Chambrier, A.K. Ray, M.J. Deen, Evolutionary computation for parameter extraction of organic thin-film transistors using newly synthesized liquid crystalline nickel phthalocyanine, Micromachines 10 (10) (2019) 683.
[87] S. Luke, ECJ then and now, in: Proc. of the GECCO, GECCO '17, ACM, New York, NY, USA, 2017, pp. 1223–1230.
[88] M. Kitamura, Y. Arakawa, Pentacene-based organic field-effect transistors, J. Phys.-Condens. Mater. 20 (18) (2008) 184011.
[89] B. Stadlober, M. Zirkl, M. Beutl, G. Leising, S. Bauer-Gogonea, S. Bauer, High-mobility pentacene organic field-effect transistors with a high-dielectric-constant fluorinated polymer film gate dielectric, Appl. Phys. Lett. 86 (24) (2005) 242902.